Ceramics International 48 (2022) 29136–29143

Contents lists available at ScienceDirect

Ceramics International

journal homepage: www.elsevier.com/locate/ceramint

Hierarchical $BaTiO_3/NiFe_2O_4$ nanocomposite as an efficacious photoanode for photoelectrochemical water splitting

Hemalatha Parangusan [a], Jolly Bhadra [a,*], Zubair Ahmad [a], K. Karuppasamy [c], Shoaib Mallick [b], Farid Touati [b], Noora Al-Thani [a]

[a] Qatar University Young Scientist Center (QUYSC), Qatar University, P.O. Box 2713, Doha, Qatar
[b] Department of Electrical Engineering, College of Engineering, Qatar University, P.O. Box 2713, Doha, Qatar
[c] Division of Electronics and Electrical Engineering, Dongguk University-Seoul, Seoul, 04620, Republic of Korea

ARTICLE INFO

Keywords:
Hierarchical nanocomposite
$BaTiO_3/NiFe_2O_4$
Photocatalyst
Water splitting

ABSTRACT

Photocatalysis of water for the production of oxygen and hydrogen is one of the most important development in the drive for clean energy, and it has received a lot of attention because it is a green and easy step to generate fuels. Developing a more efficient, chemically stable, green and cost-effective catalytic devices for commercial use still remains a challenging task. In this research work, we have designed a new kind of hetero nanostructured hierarchical electrode $BaTiO_3/NiFe_2O_4$ composite by facile hydrothermal process. The sluggish oxygen-evolving reaction is one of the major challenge in water technology (OER). The prepared photocatalyst exhibited excellent photocatalytic activity towards OER. The prepared electrodes' physicochemical behaviors have been studied using a variety of spectroscopic techniques include powder X-ray diffraction, UV–Vis diffuse reflectance spectroscopy, X-ray photoelectron spectroscopy and Transmission electron microscopy. The HR-TEM results of pristine $BaTiO_3$ show partially agglomerated nanoparticles which are in spherical shape with size ranging from 50 to 78 nm, whereas pure $NiFe_2O_4$ displays needle-like nanorods with average width and length of the needles are around 31 nm and 1.5 μm respectively and the $BaTiO_3/NiFe_2O_4$ composite shows combination of nanoparticles with nanorods. XPS analysis has revealed the oxygen vacancies and composition of the materials. The optical band gap investigation showed that the composites E_g value is in the visible region. UV–Vis diffuse reflectance spectroscopy revealed that the hierarchical $BaTiO_3/NiFe_2O_4$ composite has enhanced absorption in the visible region. The photocatalytic activity results show that, the prepared $BaTiO_3/NiFe_2O_4$ composite photoelectrode yields a photocurrent density of 0.34 mA/cm^2 at 1.6 V vs SCE reference electrode confirms their PEC water splitting ability. These observed findings of the hetero-composite clearly make a way to employ them as the plausible electrode for effectual oxygen evolution reaction.

1. Introduction

In the past few years, the demand for energy consumption and environmental pollution issues have urged the researchers to focus on the clean and efficient energy to replace the fossil fuels consumptions. As an alternative to fossil fuels, hydrogen is one of the clean and renewable energy resource. Hydrogen is a typical sustainable and clean fuel that is produced by two electron transfer from water splitting [1–3]. The hydrogen production by photoelectrochemical water splitting (PEC) is considered to be an efficient and inexpensive method to meet the future energy requirements [4,5]. However, the other half-cell reaction of water splitting is oxygen evolution reaction (OER) which is kinetically sluggish and requires higher overpotential to produce O_2 with four electron transfer ($2H_2O_{(l)} \rightarrow O_{2(g)} + 4e^- + 4H^+$ (1); $4H^+_{aq} + 4e^- \rightarrow 2H_2$ (2)). Henceforth, to overcome the kinetic barrier as well as sluggish kinetics at electrode-electrolyte interface, a large overpotential is required [6,7]. In this regard, various semiconductor based photocatalysts such as TiO_2, ZnO, ZnS, CdS have been developed as photocatalyst for photocatalytic water splitting in the past years [8,9]. However, these materials show disadvantages include a wide band gap that can be active only in the UV irradiation, fast recombination of charge carriers which are also prone to photocorrosion [10]. In order to overcome these problems, the researchers have focused the direction towards the development of high efficiency water splitting

* Corresponding author.
E-mail address: jollybhadra@qu.edu.qa (J. Bhadra).

https://doi.org/10.1016/j.ceramint.2022.05.063
Received 17 April 2022; Received in revised form 4 May 2022; Accepted 6 May 2022
Available online 12 May 2022

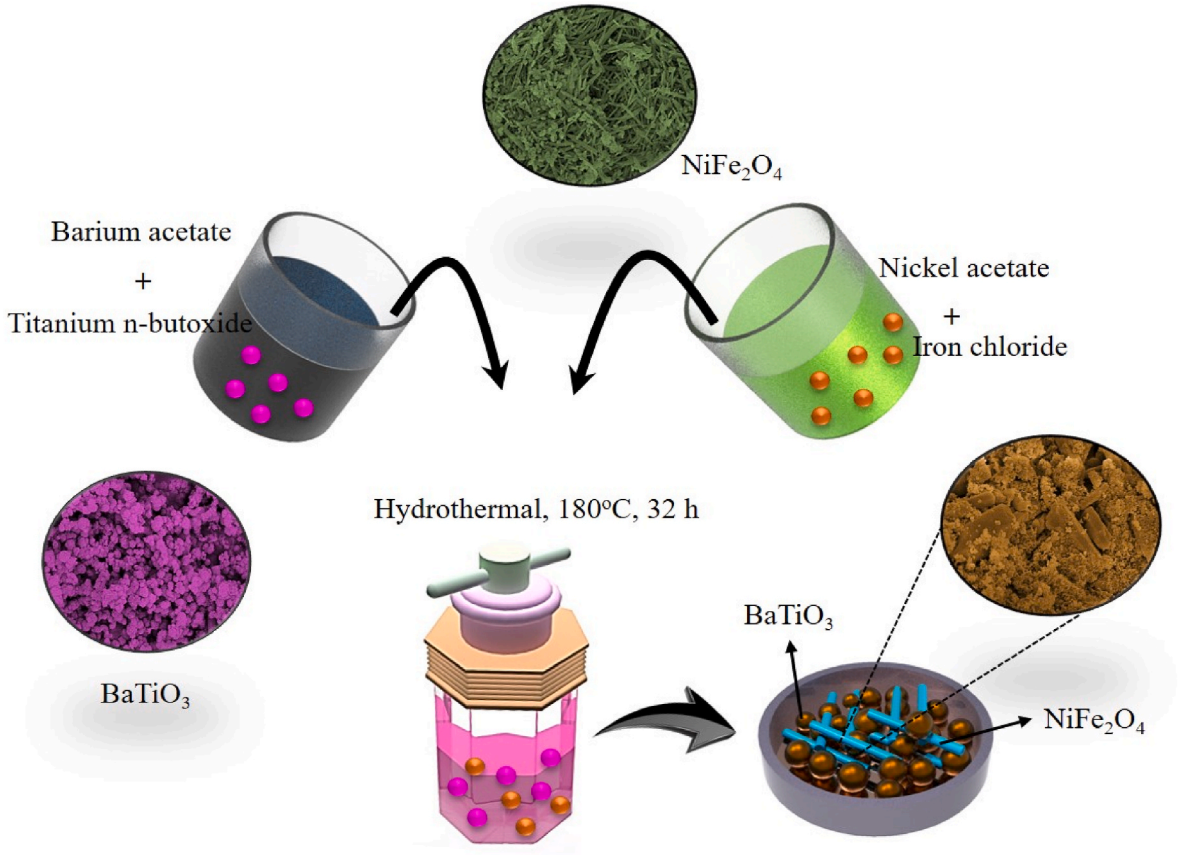

Fig. 1. Schematic diagram of facile hydrothermal processes for the preparation of $BaTiO_3/NiFe_2O_4$ composite electrode.

photoelectrodes in the recent years.

Recently, perovskite materials are gaining a great deal of interest in photocatalytic application owing to their valence and vacancy control [11]. Among the various materials studied, Barium titanate ($BaTiO_3$) perovskite material has employed as the promising photoelectrode for PEC water splitting due to their lack of photocorrosion in aqueous media [12]. However, $BaTiO_3$ is having certain drawbacks such as low absorption of visible light and fast recombination of electron-hole pairs. To improve the photocatalytic activity of $BaTiO_3$, various attempts have been made, such as nanostructuring, surface modification, chemical doping, and heterojunction construction [13,14]. The nanocomposite-based materials are an effective way to improve the photo-induced charge separation and the absorption of solar light from UV to visible light. Combination of $BaTiO_3$ with Cu_2O reduced the recombination of photo generated charge carriers and enhanced the absorption in visible light [12]. When $BaTiO_3$ was coupled with $CaFe_2O_4$, that reduced the recombination of photo generated charge carriers and enhanced the photo response [15] which in turns to improve the photocatalytic activity of $BaTiO_3/CaFe_2O_4$. In addition, $Fe_3O_4/BaTiO_3$ and $BaTiO_3/C_3N_4$ composites showed enhanced photocatalytic activity owing to its high absorption and the higher separation of charge carriers [16,17].

Herein, we design a new category of nanocomposite electrode that comprising of $BaTiO_3/NiFe_2O_4$ through facile hydrothermal process and studied their photo electrochemical activity in 1 M KOH medium. The prepared composite electrodes were characterized by different physicochemical and PEC water-splitting analyses. Further, it exhibited the maximum photocurrent density of 0.35 mA/cm^2 at an over potential of 1.6 V vs SCE reference electrode.

2. Experimental procedure

2.1. Materials

Barium acetate (($C_4H_6BaO_4$), M_w = 255.43), nickel nitrate ((Ni$(NO_3)_2{\cdot}6H_2O$, M_w = 290.81), iron chloride ($FeCl_3{\cdot}6H_2O$, M_w = 270.30) and potassium hydroxide were obtained from Sigma Aldrich and used as such. Titanium(IV) n-butoxide (($C_{16}H_{36}O_4$)Ti, M_w =340.35) was purchased from Fisher Scientific. Ethanol (C_2H_5OH, M_w = 46.07) was obtained from Sigma Aldrich and used without distillation.

2.2. Preparation of $BaTiO_3/NiFe_2O_4$ photocatalyst

Pure $BaTiO_3$, $NiFe_2O_4$ and $BaTiO_3/NiFe_2O_4$ composites were prepared by the hydrothermal method [18]. Their corresponding schematic representation is provided in Fig. 1. Initially, a required 0.06 M amount of nickel nitrate and iron chloride were prepared using deionized water and mixed together through mechanical agitation. Then, titanium (IV) n-butoxide (0.04 M) was dissolved in ethanol, and then 0.04 M barium acetate was added into it. Then, both solutions were mixed and stirred well for 2 h until a homogeneous solution was obtained. The pH was maintained at 13 by adding the KOH solution (0.1 M). The resultant solution was then transferred into Teflon lined steel autoclave at a temperature of 180 °C for 32 h. Finally, the precipitate thus obtained was washed with distilled water and ethanol and then dried at 80 °C for 6 h.

2.3. Characterization methods

Transmission electron microscopy (TEM, Phillips CM 12) was used to analyze the surface morphology of the prepared electrode samples. The various chemical states and composition of different elements on the

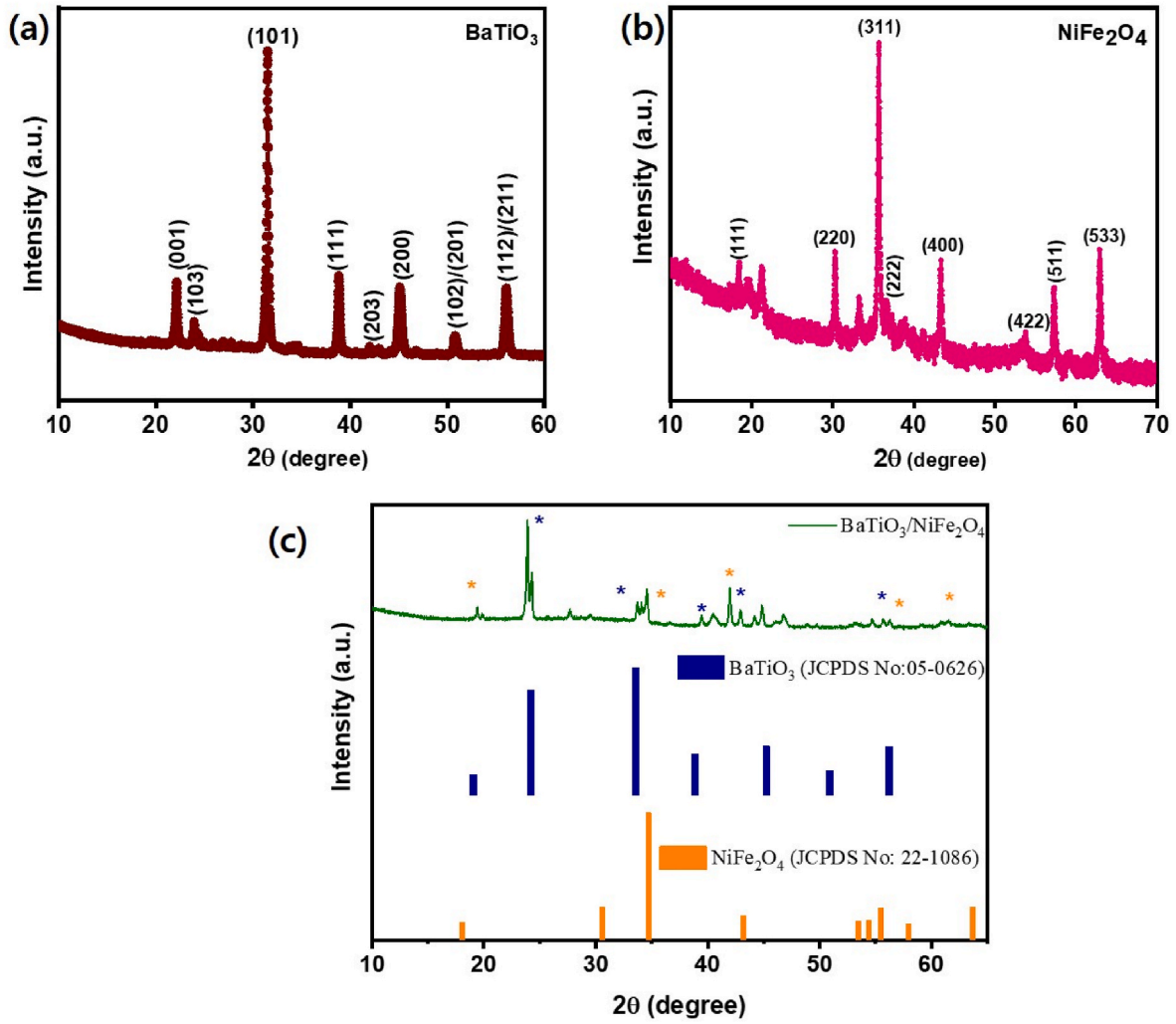

Fig. 2. X-ray diffraction pattern of (a) pure $BaTiO_3$, (b) $NiFe_2O_4$ and (c) $BaTiO_3/NiFe_2O_4$ composite compared with JCPDS data of $NiFe_2O_4$ (JCPDS No: 22–1086) and $BaTiO_3$ (JCPDS No: 05–0626).

electrode's surface were evaluated by X-ray photoelectron spectroscopy using (Kratos AXIS Ultra DLA). X-ray powder diffraction (XRD) patterns for the composite powders were recorded using Empyrean, Panalytical, UK to determine the samples crystalline nature. Biocrom Libra S 70 spectrophotometer was used to record UV–vis absorbance spectra to study the absorption behavior and band gap of the prepared electrode samples.

2.4. Photoelectrochemical characterization

Preparation of electrodes: 5 mg of photocatalyst was dispersed in mixed solution that contained 475 μL of isopropyl alcohol and 25 μL Nafion solution under ultra-sonication process. 4 μL of the slurry was spread on the polished glassy carbon electrode using micro pipette and the electrode was allowed to dry at room temperature.

Photoelectrochemical measurements: A three-electrode cell configuration was used for photo electrochemical measurements, with a saturated calomel electrode (SCE) as the reference electrode and graphite rod as the counter electrode. The prepared $BaTiO_3/NiFe_2O_4$ composite was acted as a working electrode and the electrolyte used for photo electrochemical water splitting was 1 M KOH.

3. Results and discussion

The powder X-ray diffraction patterns of pure $BaTiO_3$, $NiFe_2O_4$ and $BaTiO_3/NiFe_2O_4$ composite are shown in Fig. 2(a–c). The diffraction peaks of $BaTiO_3$ that appeared at $2\theta = 22.0°$, 24.1°, 31.4°, 38.8°, 41.9°, 45.0°, 50.8° and 56.1° corresponds to the crystalline planes of (001), (103), (101), (111), (203), (200), (102)/(201) and (112/211) respectively, of tetragonal $BaTiO_3$, which are in concurrent with the standard data (JCPDS 05–0626). For $NiFe_2O_4$ sample, the diffraction peaks located at 2θ =18.5°, 30.2°, 35.8°, 36.6°, 43.4°, 53.7°,57.3° and 63.0° corresponds to the (111), (220), (311), (222), (400), (422), (511) and (533), crystalline planes of cubic-spinel structure $NiFe_2O_4$ (JCPDS 22–1086). The XRD pattern of $BaTiO_3/NiFe_2O_4$ composite shows the distinct peaks for both $BaTiO_3$ and $NiFe_2O_4$, which confirms the formation of the composite structure. Further, in the XRD pattern, no other impurities or minor peaks were observed, which indicates the purity of the composite composed by the $BaTiO_3$ and $NiFe_2O_4$ through the hydrothermal method.

The presence of sharp diffraction peaks indicating that the prepared samples have a good crystalline nature.

SEM images and EDX spectra of the Pure $BaTiO_3$, $NiFe_2O_4$ and $BaTiO_3/NiFe_2O_4$ composites are presented in Fig. 3(a-f). Fig. 3a shows the pure $BaTiO_3$ sample, it consists of spherical nanoparticles. From Fig. 3b, we can see that $NiFe_2O_4$ are nanorod like structure. Fig. 3c, indicate that the $BaTiO_3/NiFe_2O_4$ composite is formed by the $BaTiO_3$ and $NiFe_2O_4$. The results of EDX analysis in Fig. 3d-f confirmed the elemental compositions of Ba, Ni, Fe, Ti and O without any impurity in the $BaTiO_3/NiFe_2O_4$ composite. The EDX peaks of pure $BaTiO_3$ and

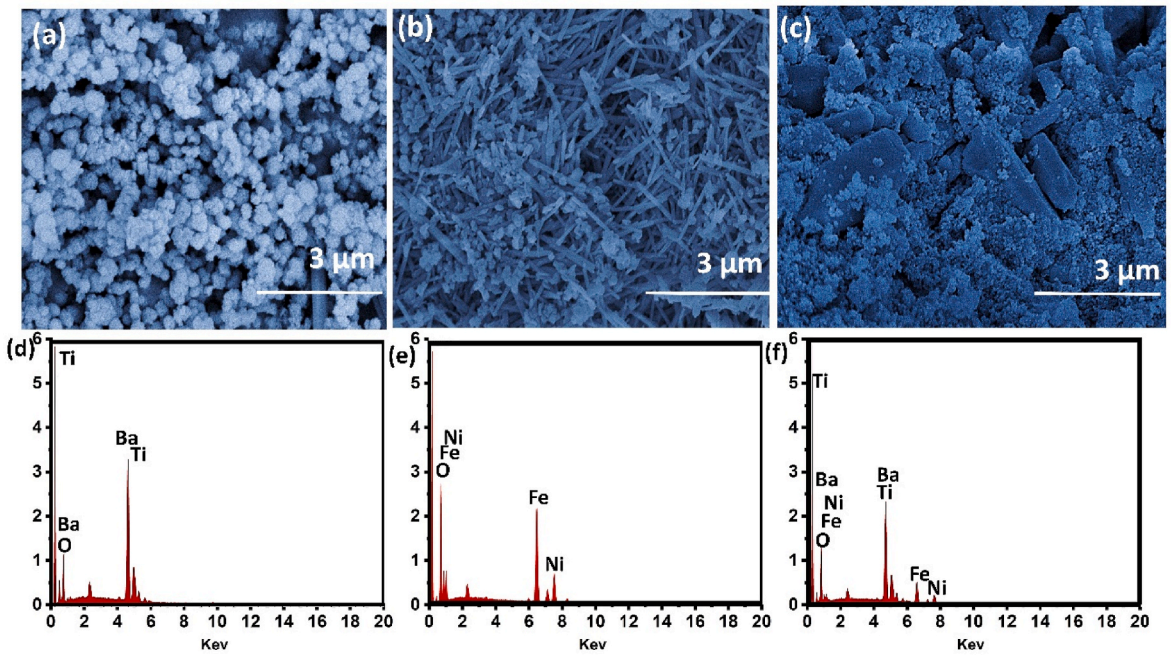

Fig. 3. SEM images and EDX spectrum of (a, d) pure $BaTiO_3$, (b, e) $NiFe_2O_4$ and (c, f) $BaTiO_3/NiFe_2O_4$ composite.

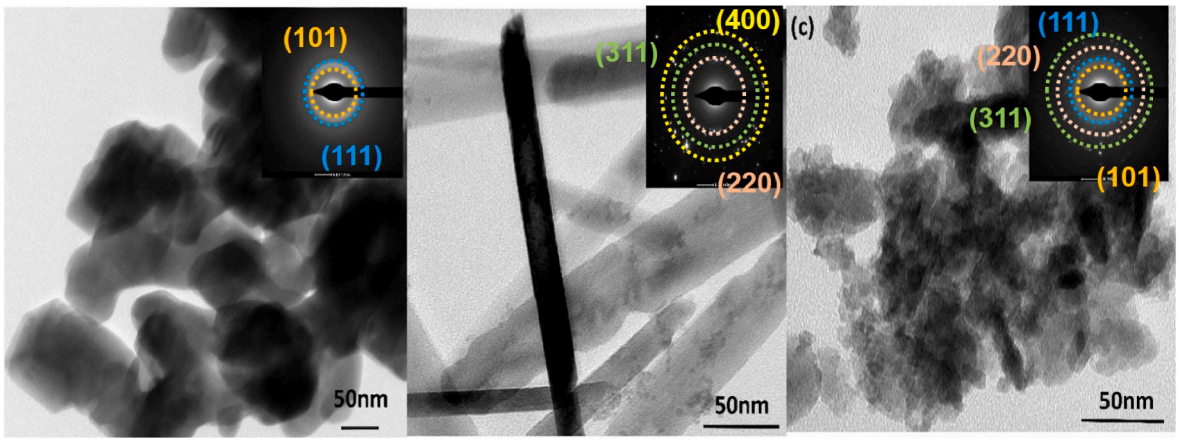

Fig. 4. TEM images of (a) $BaTiO_3$, (b) $NiFe_2O_4$ and (c) $BaTiO_3/NiFe_2O_4$ (inset: their corresponding SAED pattern).

$NiFe_2O_4$ samples are attributed to Ba, Ti, Ni, Fe and O elements (Fig. 3d, e).

To further investigate the morphologies of the prepared samples, transmission electron microscopy (TEM) analysis has been carried out and the results are depicted in Fig. 4(a–c). Fig. 4a shows the pure $BaTiO_3$ sample, it consists of partially agglomerated spherical nanoparticles with the size ranging from 50 to 78 nm. The inset of Fig. 4a shows the selected area diffraction pattern (SAED) and it can be indexed to tetragonal structure of $BaTiO_3$ nanoparticles. Fig. 4b shows the pure $NiFe_2O_4$, it displays well organized nanorods and its width and length of the rods are found to be 31 nm and 1.5 μm respectively. Their corresponding SAED pattern belongs to the cubic spinel structure. Fig. 4c shows the TEM image of $BaTiO_3/NiFe_2O_4$ composite which shows combination of nanoparticles with nanorods in which the dark section corresponds to $BaTiO_3$ particles and light grey sections are attributed to $NiFe_2O_4$ nanorods. The relevant SAED pattern is provided and their corresponding planes of $BaTiO_3$ and $NiFe_2O_4$ are indexed in the inset of Fig. 4c. In the diffraction pattern, the various colors dots indicate the planes of $NiFe_2O_4$ and the diffraction rings correspond to $BaTiO_3$ nanoparticles.

The surface chemical composition and valence charge states of the synthesized $BaTiO_3$, $NiFe_2O_4$ samples are identified using XPS measurements. The detailed XPS analysis is shown in Fig. 5. Fig. 5a shows the XPS survey spectra for $BaTiO_3/NiFe_2O_4$, confirming Ba, Ti, Ni, Fe and O presence in as prepared $BaTiO_3/NiFe_2O_4$ composites. The deconvolution of Ba 3d spectrum (Fig. 5b) indicates a perfect fit to four peaks located at the binding energies of 777.1 eV, 778.5 eV, 793.9 eV and 792.5 eV. The peaks located at the BE of 777.1 and 793.9 eV attributed to the Ba $3d_{5/2}$ and Ba $3d_{3/2}$, respectively, 3d core level of Ba ions. The other two represent their respective shoulder peaks. These four peaks attributed to the existence of Ba^{2+} and Ba^{4+} valence state of Ba.

In the Ti_{2p} XPS spectrum shows two strong signals at the binding energies of 454.5 eV and 460.2 eV which corresponds to the Ti $2p_{3/2}$ and Ti $2p_{1/2}$ respectively as displayed in Fig. 5c [19]. The fitted Ti_{2p} spectrum confirms the existence of Ti in +3 and + 4 oxidation state. Moreover, the BE of Ti_{2p} is located at 454.5 eV, which is smaller than that reported for $BaTiO_3$ bulks. This downshift of the BE indicates that the oxidation state of Ti in $BaTiO_3$. These result indicate that there are some structural defects in the sample and these are due to local oxygen vacancies in the synthesized materials [20]. As shown in Fig. 5d, the

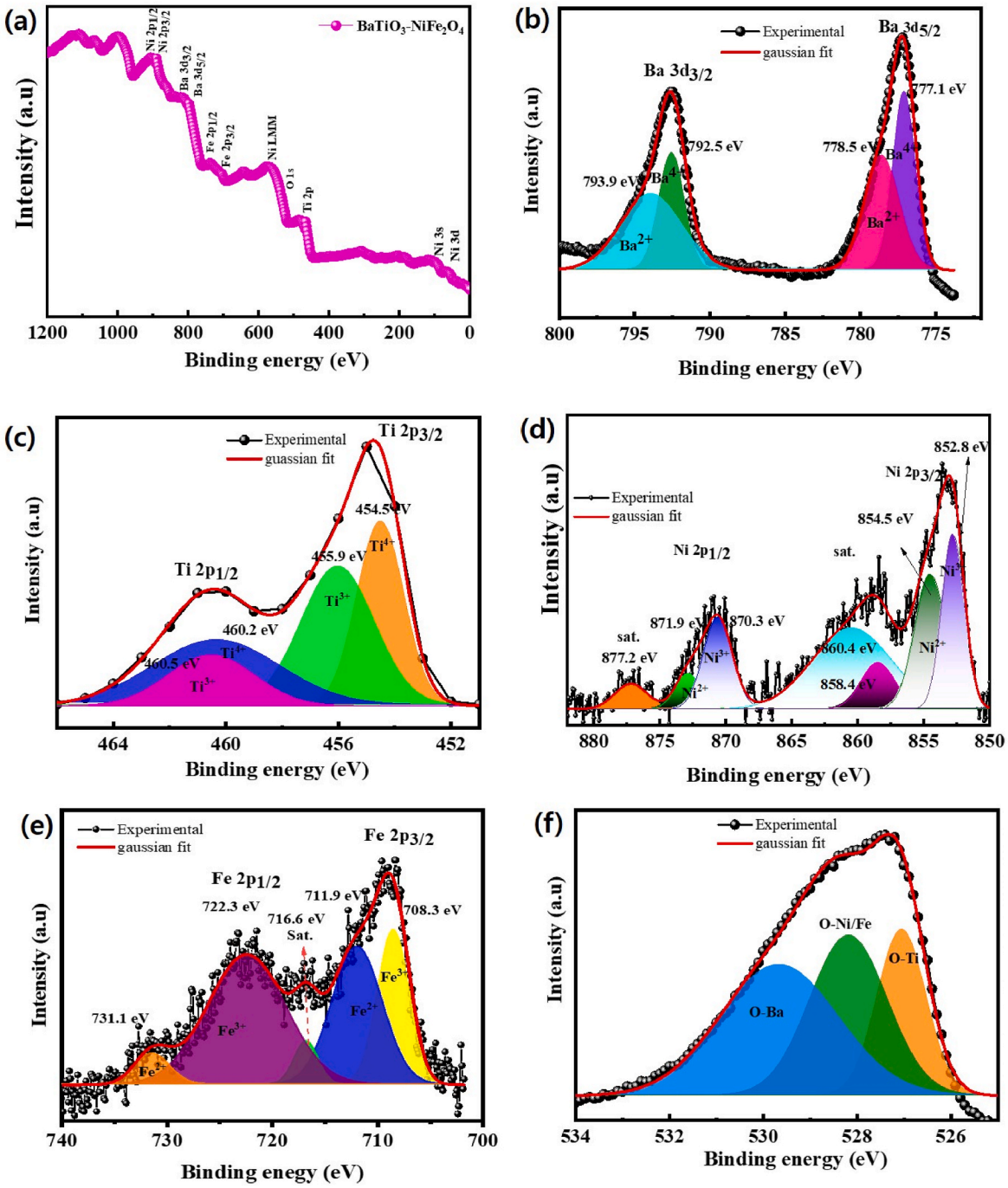

Fig. 5. (a) XPS survey spectrum and XPS core level for (b) Ba 3d, (c) Ti 2p, (d) Ni 2p, (e) Fe 2p and (f) deconvolution spectrum of O 1s of composite $NiFe_2O_4/BaTiO_3$.

ultra-high signals at binding energies of 854.5 and 871.9 eV can be attributed to Ni $2p_{3/2}$ and Ni $2p_{1/2}$, indicating the presence of Ni^{2+}. The other two deconvoluted peaks represent their respective shoulder peaks. Similarly, the Fe 2p (Fig. 5e) also shows the existence of mixed valence of Fe in +2 and + 3 form. [21]. The O 1s spectrum (Figure 5f) is further deconvoluted into three peaks at 530.1, 528.1 and 527.0 eV. These characteristic peaks are assigned to the lattice oxygen in the metal oxide structure and the presence of H_2O adsorbed on the particle surface [22].

The light absorption properties of the materials are one of the significant key parameters for acieving high efficiency in solar water splitting. UV–Vis diffuse reflectance spectar (DRS) is used to analyze the optical absorption properties of pure $BaTiO_3$, $NiFe_2O_4$ and $BaTiO_3$/$NiFe_2O_4$ composite and it is shown in Fig. 6. The optical absorption spectra is represented in Fig. 6a. Pure $NiFe_2O_4$ and $BaTiO_3$ have showed the absorption bands at aorund 300 and 277 nm in the UV region. The UV–vis absorption spectra of the composite shows stronger and broder peaks in the region from 300 to 500 nm, compared with the pure $BaTiO_3$ and $NiFe_2O_4$ which may owing to the electrostatic interaction and oxygen deficiency in the composite crystal structure [23]. Further, the absorption edge of composite sample has expanded into visible region and shows a red shift compared with pure $BaTiO_3$ and $NiFe_2O_4$ samples.

The optical band gap energy (E_g) of the composite is determined using the following equation.

$$(\alpha h\nu)^n = A\left(h\nu - E_g\right) \quad (1)$$

Where h is the Planck's constant and A is the characteristics parameter

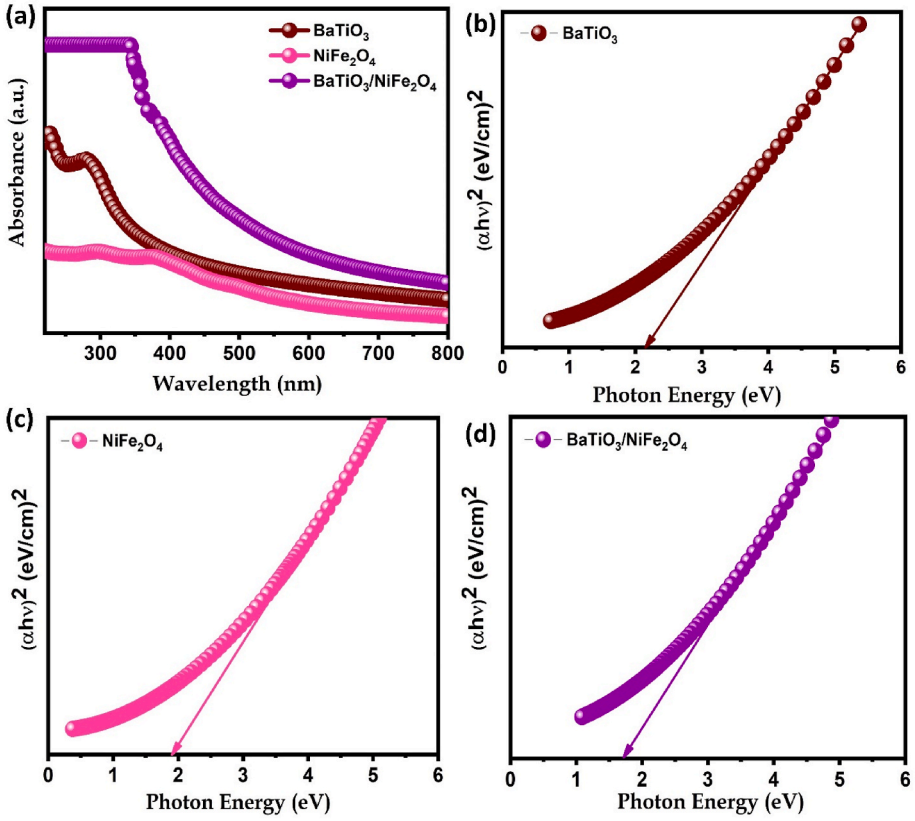

Fig. 6. (a) UV–vis absorption spectra and Tauc's plot of (b) $BaTiO_3$, (c) $NiFe_2O_4$, (d) $BaTiO_3/NiFe_2O_4$ composite.

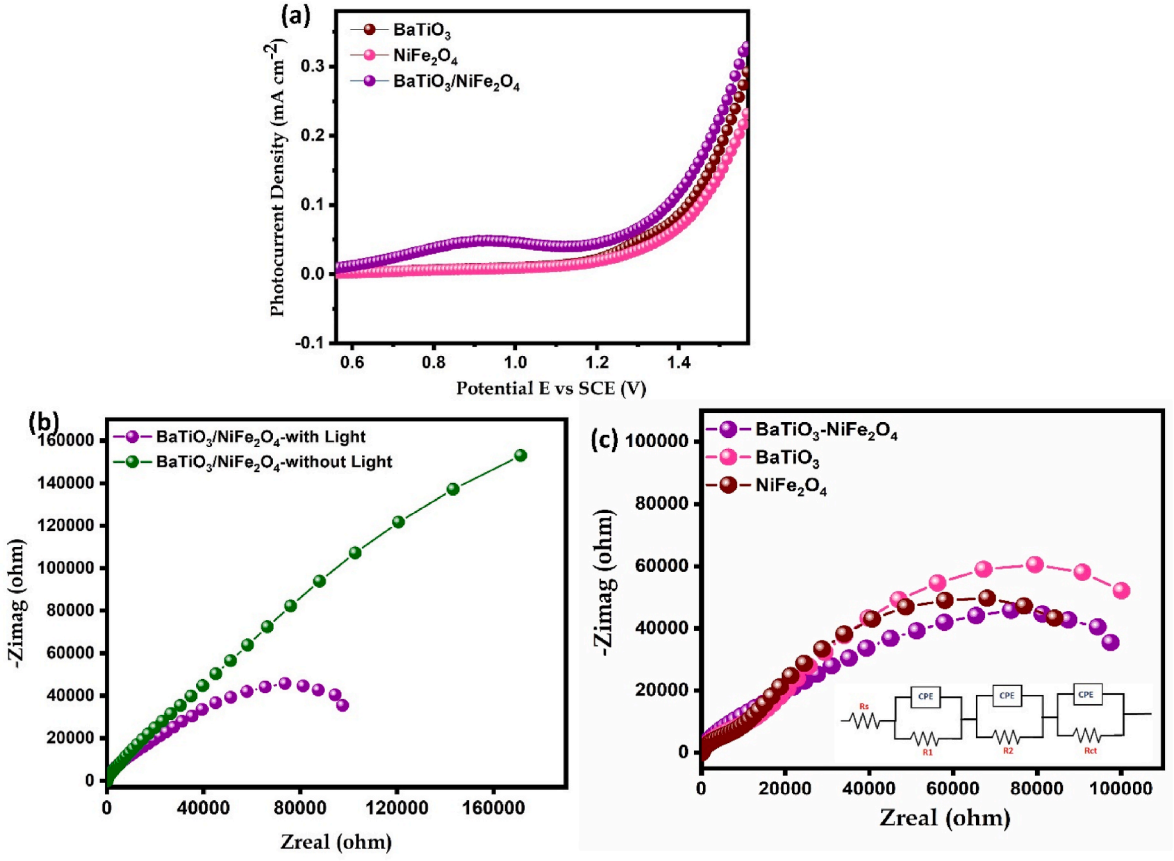

Fig. 7. (a) LSV polarization curve and (b, c) EIS spectrum of $BaTiO_3$, $NiFe_2O_4$ and $BaTiO_3/NiFe_2O_4$.

Table 1
Impedance Fitting values of R_1, R_2 and R_{ct} of $BaTiO_3$·$NiFeO_3$ and BaTiO3–$NiFeO_3$ composite.

Materials	Rs	R_1	R_2	R_{ct}	Goodness to fit
$BaTiO_3$	17.52	17.52×10^3	20	172.1×10^3	1.92×10^{-3}
$NiFeO_3$	10.68	10.96×10^3	300.7	160×10^3	3.291×10^{-3}
$BaTiO_3$–$NiFe_2O_4$	13.47	120.1	65.75×10^3	106.3×10^3	789.9×10^{-6}

for this transition. The exponent 'n' characterizes the value ½ for the allowed indirect transition and 2 for the allowed direct transition. Tauc's plots is used to calculate the band gap of the prepared samples as shown in Fig. 6(b–d). The optical energy bandgap (E_g) value is estimated by extrapolating the linear part on the X-axis. The calculated energy band gap values for pure $BaTiO_3$, NiF_2eO_4 and $BaTiO_3$/$NiFe_2O_4$ are found to be 2.32 eV, 1.81 eV and 1.62 eV. It can be seen that the composite has a slightly lower narrow band gap than the pure samples. These values demonstrated that the obtained samples exhibit a srong absorption in both UV and visible light regions.

3.1. Photoelectrochemical (PEC) properties

The PEC water splitting of the pristine as well as $BaTiO_3$/$NiFe_2O_4$ composite samples have been investigated by using linear sweep voltammetry (LSV) under simulated sunlight irradiation. Fig. 7a shows the LSV of the $BaTiO_3$, $NiFe_2O_4$ and $BaTiO_3$/$NiFe_2O_4$ composite. The composite based photoanode yields a photocurrent density of 0.34 mA/cm^2 at 1.6 V vs SCE reference electrode, while the photocurrent of pure $BaTiO_3$ (0.28 mA cm^{-2}) and $NiFe_2O_4$ (0.22 mA cm^{-2}). The increased photocurrent density of the composite based sample can be ascribed to the increasing of active area and light absorption. The separation of photo induced electron-hole pairs and enhanced visible light absorption at the photoanode and electrolyte interface are the reasons for an enhancement of photocurrent density. The composite sample can enhance the light absorption in visible region due to its narrow band gap compared to $BaTiO_3$ and $NiFe_2O_4$ samples.

The surface defect such as oxygen vacancy play a significant role on the PEC performance of the samples [24] which can be acted as a trap center for the excited electrons. In our case, the surface oxygen vacancy and narrowing band gap have showed an impact on the photoelectrochemical properties which in turn corroborate with the results obtained by XPS and UV–Vis analyses. .

The electrochemical impedance spectroscopy (EIS) measurement is an effective method to study electrochemical behavior, especially charge transfer phenomena at the electrode-electrolyte interface. Fig. 7b shows the Nyquist impedance curve of the $BaTiO_3$–$NiFe_2O_4$ composite in 1 M KOH solution under dark and simulated in sunlight irradiation in the frequency range of 100 kHz–100 MHz. From the figure, it is observed that the Nyquist curve semi-circle under light has comparatively smaller diameter than that in the dark, indicating improved separation of the charge carrier under light irradiation [25]. Fig. 7c shows the Nyquist curve for $BaTiO_3$, $NiFe_2O_4$, and $BaTiO_3$–$NiFe_2O_4$ composite under simulated sunlight irradiation. It can be observed from the figure that the semi-circle of the Nyquist curve of $BaTiO_3$–$NiFeO_3$ composite is much smaller than $BaTiO_3$ and $NiFe_2O_4$ alone. This decrease in diameter increases the efficiency of the transfer and separation of photo-created electrons and holes, enabling the photocatalyst's improved efficiency [26].

The inset in Fig. 7c shows the equivalent circuit (three RC circuit) use to simulate the impedance response of $BaTiO_3$, $NiFe_2O_4$, and $BaTiO_3$–$NiFe_2O_4$ composite to evaluate the charge transfer resistance (R_{ct}) by fitting the Nyquist curve of $BaTiO_3$, $NiFe_2O_4$, and $BaTiO_3$–$NiFe_2O_4$ composite and it is shown in Table 1. The R_{ct} of $BaTiO_3$, $NiFe_2O_4$, and $BaTiO_3$–$NiFe_2O_4$ composite are computed to be 172.1 $\times10^3$, 160×10^3, and 106.3 $\times10^3$, Ω respectively. The various electrochemical parameter fitting values are shown in Table 1. The decrease in charge transfer resistance of $BaTiO_3$–$NiFe_2O_4$ composite increases the charge transfer rate at the electrode and electrolyte surface. The mechanism of charge transfer in $BaTiO_3$–$NiFe_2O_4$ composite minimizes the recombination rate of electron-hole pairs; as a result, the availability of hole and electron increased the photocatalytic reaction [16].

4. Conclusion

In the present investigation, a series of photoelectrodes such as $BaTiO_3$, $NiFe_2O_4$ and $BaTiO_3$–$NiFe_2O_4$ composite have been prepared by facile hydrothermal approach and employed them as the promising electrodes for PEC water splitting. The morphological features of the composite sample has revealed that it consisted of hierarchical combination of nanoparticles along with nanorods. As compared to bare $BaTiO_3$, and $NiFe_2O_4$ samples, the composite sample has exhibited narrow band gap which indicates its srong absorption properties in both UV and visible light regions. The composite photoanode yields a photocurrent density of 0.34 mA/cm^2 at 1.6 V, while the photocurrent of pure $BaTiO_3$ (0.28 mA cm-2) and $NiFe_2O_4$ (0.22 mA cm-2) which in turns to suggest it as an alternative promising photoanode for PEC water splitting and clean H_2 energy production.

Declaration of competing interest

The authors declare that they have no known competing financial interests or personal relationships that could have seemed the work reported in this paper.

Acknowledgement

This work is supported by Qatar University Internal Grant having project number QUCG-CAM-20/21–6. The findings achieved herein are solely the responsibility of the authors. The characterizations of this work are accomplished in the Central Laboratories unit, Qatar University. A part of the characterization has been accomplished in the Gas Processing Center.

References

[1] K. Karuppasamy, Vasanth Rajemdiran Jothi, Dhanasekaran Vikraman, K. Prasanna, T. Maiyalagan, Byoung-In Sang, Sung-Chul Yi, Hyun-Seok Kim, Metal-organic framework derived NiMo polyhedron as an efficient hydrogen evolution reaction electrocatalyst, Appl. Surf. Sci. 478 (2019) 916–923.
[2] K. Karuppasamy, Ranjith Bose, Vasanth Rajendiran Jothi, Dhanasekaran Vikarman, Yen-Tae Jeong, Paulraj Arunkumar, Dhinesh Babu Velusamy, T. Maiyalagan, Akram Alfantazi, Hyun-Seok Kim, High performance, 3D-hierarchical CoS_2/CoSe@C nanohybrid as an efficient electrocatalyst for hydrogen evolution reaction, J. All. Com. 838 (2020), 155537.
[3] Y. Lee, J. Suntivich, K.J. May, E.E. Perry, Y. Shao-Horn, Synthesis and activities of rutike IrO_2 and RuO_2 nanoparticles for oxygen evolution in acid and alkaline solutions, J. Phys. Chem. Lett. 3 (2012) 399–404.
[4] S.J. Moniz, S.A. Shevlin, D.J. Martin, Z.-X. Guo, J. Tang, Visible-light driven heterojunction photocatalysts for water splitting–a critical review, Energy Environ. Sci. 8 (3) (2015) 731–759.
[5] M. Ni, M.K. Leung, D.Y. Leung, K. Sumathy, A review and recent developments in photocatalytic water-splitting using TiO_2 for hydrogen production, Renew. Sustain. Energy Rev. 11 (3) (2007) 401–425.
[6] L. Duan, F. Bozoglian, S. Mandal, B. Stewart, T. Privalov, A. Liobet, L. Sun, A molecular ruthenium catalyst with water oxidation activity comparable to that of photosystem II, Nat. Chem. 4 (2012) 418–423.
[7] C.C. McCrory, S. Jung, I.M. Ferrer, S.M. Chatman, J.C. Peters, T.F. Jaramillo, Benchmarking hydrogen evolving reaction and oyxgen evolving reaction electrocatalysts for solar water splitting devices, J. Am. Chem. Soc. 137 (2015) 4347–4357.

[8] A. Kudo, M. Sekizawa, Photocatalytic H2 evolution under visible light irradiation on Ni-doped ZnS photocatalyst, Chem. Commun. 15 (2000) 1371–1372.
[9] Q. Li, B. Guo, J. Yu, J. Ran, B. Zhang, H. Yan, J.R. Gong, Highly efficient visible-light-driven photocatalytic hydrogen production of CdS-cluster-decorated graphene nanosheets, J. Am. Chem. Soc. 133 (28) (2011) 10878–10884.
[10] P.V. Kamat, Photochemistry on nonreactive and reactive (semiconductor) surfaces, Chem. Rev. 93 (1) (1993) 267–300.
[11] K. Kanade, J.-O. Baeg, K.-j. Kong, B. Kale, S.M. Lee, S.-J. Moon, C.W. Lee, S. Yoon, A new layer perovskites $Pb_2Ga_2Nb_2O_{10}$ and $RbPb_2Nb_2O_7$: an efficient visible light driven photocatalysts to hydrogen generation, Int. J. Hydrogen Energy 33 (23) (2008) 6904–6912.
[12] D. Sharma, S. Upadhyay, V.R. Satsangi, R. Shrivastav, U.V. Waghmare, S. Dass, Nanostructured $BaTiO_3/Cu_2O$ heterojunction with improved photoelectrochemical activity for H2 evolution: experimental and first-principles analysis, Appl. Catal. B Environ. 189 (2016) 75–85.
[13] M. Rioult, H.l.n. Magnan, D. Stanescu, A. Barbier, Single crystalline hematite films for solar water splitting: Ti-doping and thickness effects, J. Phys. Chem. C 118 (6) (2014) 3007–3014.
[14] M. Wang, M. Pyeon, Y. Gönüllü, A. Kaouk, S. Shen, L. Guo, S. Mathur, Constructing Fe_2O_3/TiO_2 core–shell photoelectrodes for efficient photoelectrochemical water splitting, Nanoscale 7 (22) (2015) 10094–10100.
[15] N.K. Veldurthi, N.K. Eswar, S.A. Singh, G. Madras, Cooperative effect between $BaTiO_3$ and $CaFe_2O_4$ in a cocatalyst-free heterojunction composite for improved photochemical H2 generation, Int. J. Hydrogen Energy 43 (51) (2018) 22929–22941.
[16] T. Xian, H. Yang, L. Di, J. Dai, Enhanced photocatalytic activity of $BaTiO_3$@ g-C_3N_4 for the degradation of methyl orange under simulated sunlight irradiation, J. Alloys Compd. 622 (2015) 1098–1104.
[17] Y. Cui, J. Briscoe, Y. Wang, N.V. Tarakina, S. Dunn, Enhanced photocatalytic activity of heterostructured ferroelectric $BaTiO_3/\alpha$-Fe_2O_3 and the significance of interface morphology control, ACS appl.mater.interfaces. 9 (29) (2017) 24518–24526.
[18] K. Verma, M. Singh, R. Kotnala, N. Goyal, Magnetic field control of polarization/capacitance/voltage/resistance through lattice strain in $BaTiO_3$-$CoFe_2O_4$ multiferroic nanocomposite, Journal of Magn.Magn. Mater. 469 (2019) 483–493.
[19] W. Yang, Y. Yu, M.B. Starr, X. Yin, Z. Li, A. Kvit, S. Wang, P. Zhao, X. Wang, Ferroelectric polarization-enhanced photoelectrochemical water splitting in TiO_2–$BaTiO_3$ core–shell nanowire photoanodes, Nano Lett. 15 (11) (2015) 7574–7580.
[20] Y. Yang, X. Wang, C. Sun, L. Li, Structure study of single crystal $BaTiO_3$ nanotube arrays produced by the hydrothermal method, Nanotechnology 20 (5) (2009), 055709.
[21] R. Bose, V.R. Jothi, K. Karuppasamy, A. Alfantazi, S.C. Yi, High performance multicomponent bifunctional catalysts for overall water splitting, J. Mater. Chem. 8 (27) (2020) 13795–13805.
[22] H. Lv, L. Ma, P. Zeng, D. Ke, T. Peng, Synthesis of floriated $ZnFe_2O_4$ with porous nanorod structures and its photocatalytic hydrogen production under visible light, J. Mater. Chem. 20 (18) (2010) 3665–3672.
[23] J. Prakash, U. Prasad, X. Shi, X. Peng, B. Azeredo, A.M. Kannan, Photoelectrochemical water splitting using lithium doped bismuth vanadate photoanode with near-complete bulk charge separation, J. Power Sources 448 (2020), 227418.
[24] F. Andrei, I. Boerasu, R. Birjega, A. Moldovan, M. Dinescu, V. Ion, C. Mihailescu, N. Scarisoreanu, V. Leca, The effects of the oxygen content on the photoelectrochemical properties of $LaFeO_3$ perovskite thin films obtained by pulsed laser deposition, Appl. Phys. A 125 (11) (2019) 807.
[25] G. Anandhababu, Y. Huang, D.D. Babu, M. Wu, Y. Wang, Oriented growth of ZIF-67 to derive 2D porous CoPO nanosheets for electrochemical-/photovoltage-driven overall water splitting, Adv. Funct. Mater. 28 (9) (2018), 1706120.
[26] N. Khalid, Z. Israr, M. Tahir, T. Iqbal, Highly efficient Bi_2O_3/MoS_2 pn heterojunction photocatalyst for H2 evolution from water splitting, Int. J. Hydrogen Energy 45 (2020) 8479–8489.